https://doi.org/10.5194/egusphere-2026-2900
Preprint. Discussion started: 10 August 2026

Retrieval of the Depolarization Ratio of Graphite Particles Using an Aerosol Chamber

Gahyeon Park[1], Dukhyeon Kim[2], Youngmin Noh[1], Gangnam Cho[3]

[1]Division of Earth Environmental System Science, Pukyong National University, Busan 48513, South Korea
[2]Department of Basic Science, Hanbat National University, Daejeon 34158, South Korea
[3]National Institute of Environmental Research, Incheon 22689, South Korea

Correspondence to Youngmin Noh (nym@pknu.ac.kr) and Gangnam Cho (gangji@korea.kr)

Abstract. This study derives the intrinsic depolarization ratio of graphite particles using a custom-built near-field polarization light detection and ranging (LiDAR) system combined with an aerosol chamber. To minimize the inherent geometric overlap problem in typical LiDAR systems, the receiver and chamber were separated by 30 m and signals were acquired at ultrahigh spatial resolution (0.03 m). Pure graphite particles and fugitive graphite particles collected from a steel plant were individually injected into a standardized chamber using a dust feeder. Parallel and perpendicular polarized backscatter signals were then measured at a wavelength of 532 nm. Background aerosol signals in the acquired raw data were eliminated through signal preprocessing and a correction algorithm. Ultimately, the intrinsic depolarization ratio was calculated as 0.15 ± 0.01 for pure graphite and 0.16 ± 0.03 for mixed particles collected from the steel plant. The results are statistically consistent (within the margin of error). The derived optical indicators provide a scientific foundation for the future development of remote monitoring technologies that can measure fugitive dust originating from steel plants in real time.

1 Introduction

Steel plants generate various fugitive-dust types in massive quantities through multiple processes involving high temperatures, high pressures, and chemical reactions. Fugitive dust from steel plants majorly contributes to air pollution and requires industrial environmental management (Doherty et al., 2017; Dusseldorp et al., 1995; Jia et al., 2018; Amodio et al., 2013). Moreover, fugitive dust is emitted irregularly during operations and cannot be tracked to a distinct stack emission source. Monitoring the generation and dispersion of such dust is essential for mitigating its impact on the surrounding environment and human health. The impact further depends on the size, composition, and physicochemical properties of the dust particles. Graphite, a nonmetallic, carbon-based material widely utilized as an electrode material, refractory material, and lubricant in the steelmaking process, must be intensively monitored (Taylor, 1985). Despite its nonmetallic nature, graphite possesses a unique metallic luster, causing visual discomfort when dispersed into the atmosphere. Inhaled graphite induces immediate coughing or respiratory irritation and can become deposited in lung tissue during prolonged and repeated exposure, causing severe chronic pulmonary diseases such as graphite pneumoconiosis. Therefore, graphite particles pose a serious threat to

https://doi.org/10.5194/egusphere-2026-2900
Preprint. Discussion started: 10 August 2026

human health (Hanoa, 1983; Rahman, 2022). However, most research related to steel plants has focused on particulate matter (PM) and metallic particles; studies on nonmetallic particles such as graphite are limited.

Scanning Light Detection and Ranging (LiDAR) can continuously observe the spatial distribution of fugitive dust from steel plants at high resolution in real time. As a representative active remote-sensing technology, LiDAR analyzes the backscattered signals from laser light irradiated into the atmosphere, thereby determining the characteristics and distribution of atmospheric particles (Shimizu et al., 2017; Uthe, 1983; Xian et al., 2020). Scanning LiDAR provides valuable information for identifying the emission sources and dispersion pathways of fugitive dust (Ma et al., 2019; Wang et al., 2020; Xie et al., 2015; Shin et al., 2025; Pal et al., 2006; Palm et al., 1994; Scollo et al., 2012; Eberhard and Mcnice, 1986).

During its transport, graphite emitted from steel plants can be mixed with other fugitive dusts or various atmospheric aerosols. The LiDAR backscatter signals of graphite are not easily distinguished from those of other fine dust particles. To isolate the distribution of graphite, the present study utilizes the depolarization ratio (D_p), an important indicator of particle nonsphericity. Ranging from 0 (entirely spherical) to 1 (completely nonspherical), the D_p has been effectively used in various particle-classification studies. For instance, it has distinguished ice crystals from water droplets in cirrus clouds (Sassen and Benson, 2001), enabled tracking of desert dust (characterized by high D_p, typically over 0.3) during its long-range transport (Freudenthaler et al., 2009; Groß et al., 2015; Sakai et al., 2003), and identified biological particles such as pollen (Bohlmann et al., 2020; Noh et al., 2013b; Noh et al., 2013a; Shin et al., 2025).

If the D_p of a specific particle is known, the presence and contribution of that particle within mixed aerosols can be estimated from LiDAR observations. As graphite is an anthropogenic particle not naturally present in the general atmosphere, the D_p of pure graphite particles has not been previously reported. Once the intrinsic D_p of graphite has been determined, the presence of graphite among the steel-plant fugitive dusts can be detected in LiDAR data. To this end, the present authors constructed an experimental system using near-field polarization LiDAR and a chamber for measuring the D_p values of pure and actual graphite particles emitted from a steel plant. This system can detect graphite particles in the atmosphere. Section 2 describes the characteristics of the experimental graphite particles and the LiDAR-based measurement methodology. Section 3 presents the experimental results, and Section 4 synthesizes the findings, leading to the study conclusions.

2 Material and Methodology

2.1 Experimental Equipment

The optical properties of the graphite particles were measured using a custom-built near-field polarization LiDAR system (Fig. 1). The system consists of a transmitter that generates laser pulses, a receiver that collects the backscattered signals, and a data-acquisition unit that processes and records the signals. Operating organically, these components capture the real-time optical responses of particles generated within the localized space of the chamber. Table 1 summarizes the specifications and optical configurations of the constructed LiDAR system.

https://doi.org/10.5194/egusphere-2026-2900
Preprint. Discussion started: 10 August 2026

2.1.1 Transmitter

The light source of the transmitter was a Quantel Ultra Nd:YAG laser (P/N: UL332511, Les Ulis, France) with a fundamental wavelength of 1064 nm, which generates green light pulses at 532 nm via a built-in frequency-doubling unit. The output energy of the laser was set to 45 mJ per pulse, ensuring an adequate signal-to-noise ratio after accounting for the large attenuation caused by high-concentration particle groups inside the chamber. The pulse repetition rate was 10 Hz, providing 10 independent observations per second, while an external controller continuously monitored the beam quality and stability. The generated laser beam passed through a half-wave plate that controlled its polarization direction. Next, it was directed by a mirror into the center of the chamber occupied by injected graphite particles.

2.1.2 Receiver

Light backscattered by the particles inside the chamber was collected using a telescope (C5 OTA, Celestron, Torrance, CA, USA) with a 127-mm aperture and a 1250-mm focal length. The collected light was converted to parallel light through a collimation lens and then split by a polarizing beamsplitter into parallel (P-polarization) and perpendicular (S-polarization) components relative to the incident laser. Each separated signal passed through an interference filter with a full-width-at-half-maximum of 1 nm. The filter selectively transmits 532-nm light, minimizing noise from ambient light. A focusing lens focused the filtered light onto the optical surface of each channel of the detector.

2.1.3 Data Acquisition

The optical signals from each polarization channel were converted to electrical signals in a photomultiplier tube (PMT) operated by a high-voltage power supply with a maximum output of 5 kV. The minute current signals output by the PMT were amplified through an amplifier. Finally, the amplified analog signals from both channels were recorded as digital signals using an oscilloscope (WaveRunner 64Xi, Teledyne LeCroy, Chestnut Ridge, NY, USA). The ultrahigh spatial resolution (0.03 m) of the oscilloscope allows detailed observation of the particle distribution characteristics, although the chamber was only 1.2 m long. The collected waveform data were transferred to a personal computer and subsequently converted into D_p values using an algorithm developed by the research team.

https://doi.org/10.5194/egusphere-2026-2900
Preprint. Discussion started: 10 August 2026

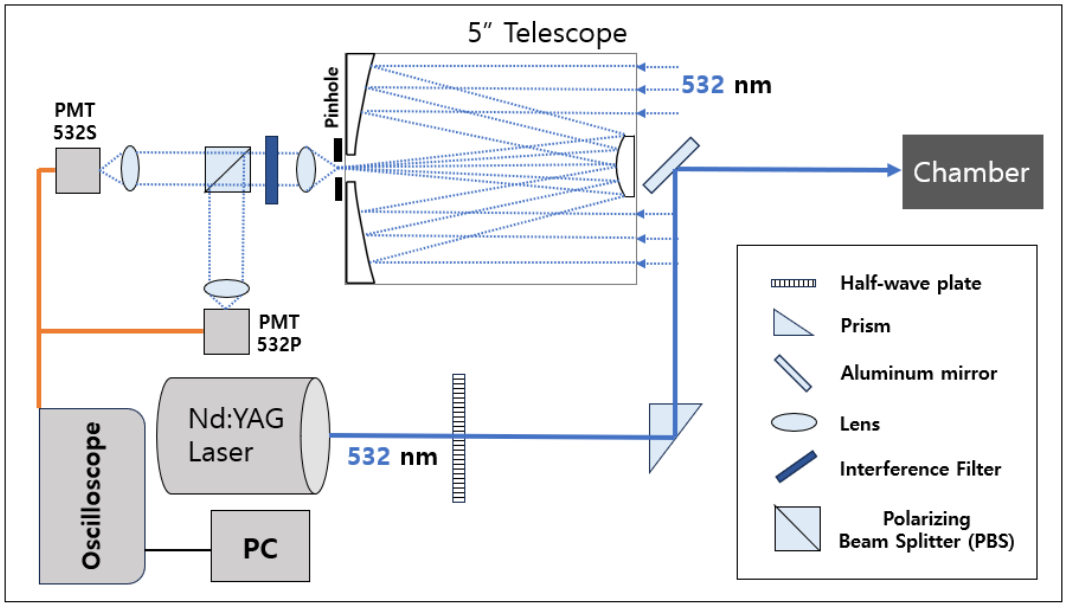

Figure 1: Schematic of the LiDAR transmitter and receiver.

Table 1: Specifications of the LiDAR system used in this study

Laser	
Type	Nd:YAG laser
Wavelength	532 nm (P, S)
Pulse Repetition	10 Hz
Power	45 mJ
Collimation Lens	Plano-convex (f = 75 mm)
Focusing Lens	Plano-convex (f = 35 mm)
Interference Filter	532 nm, FWHM 4 nm
Polarizing Beamsplitter	532 nm (Model: CCM1-PBS25-532/M)
Detector	PMT (1 cm)
Diameter of the Telescope	127 mm
Range resolution	0.03 m
A/D Converter	8-bit
Signal accumulation	30 shots (3 seconds)

https://doi.org/10.5194/egusphere-2026-2900
Preprint. Discussion started: 10 August 2026

2.2 Experimental Configuration

2.2.1 Observation Site and System Layout

Experiments were conducted on two days (June 3 and November 13, 2024) at 125 Dongseo-daero, Yuseong-gu, Daejeon, South Korea (latitude: 36.3483°, longitude: 127.3026°). As the background atmospheric conditions and meteorological factors affect the optical properties of aerosols and backscattered signals during outdoor observations, the environmental variables were monitored during the measurement periods. Air-quality data were obtained from the AirKorea urban air monitoring network (Ministry of Environment), and the meteorological data, such as temperature and wind speed, were sourced from the Automatic Weather Station data of the Korea Meteorological Administration.

The June 3 experiment was conducted around 16:00 local standard time (LST). At that time, the temperature, relative humidity, and 10-minute average wind speed were 27.1°C, 35%, and 2.7 m/s, respectively. The concentrations of PM_{10} and $PM_{2.5}$ (PM with diameters up to 10 μm and 2.5 μm, respectively) were 21 and 13 μg/m³, respectively, indicating relatively clean air conditions. The November 13 experiment began around 10:30 LST under stagnant atmospheric conditions. At this time, the temperature, relative humidity, and average wind speed were 14.8°C, 60%, and 0.3 m/s, and the PM_{10} and $PM_{2.5}$ concentrations were 48 and 32 μg/m³, respectively, reflecting a higher background aerosol load in November than in June.

The LiDAR system and chamber were separated by approximately 30 m (Fig. 2). Repeated preliminary experiments confirmed that 30 m minimizes the geometric overlap effect of the LiDAR system while securing stable backscattered signals.

Figure 2: Satellite image of the LiDAR observation site: (a) LiDAR and (b) chamber. Imagery © 2025 Airbus, Map data © 2025 Google, TMap Mobility.

https://doi.org/10.5194/egusphere-2026-2900
Preprint. Discussion started: 10 August 2026

2.2.2 Chamber and Particle Injection

The aerosol chamber used in the experiment was custom-built with dimensions of 1.2 m × 0.4 m × 0.6 m (length × width × height). The length was designed to sufficiently exceed the spatial resolution of the LiDAR system (0.03 m), ensuring that the laser pulses could generate spatially significant signals within the chamber. Graphite was injected into the chamber through a dust feeder (solid aerosol generator SAG 410, TOPAS, Dresden, Germany). The injection nozzle of the dust feeder was positioned inside the chamber, and the flow rate of the graphite powder was 2 m/s (approximately 2.5 g/h), creating a constant particle concentration in the environment. To prevent the injected particles from settling under gravity, thus maintaining a uniform suspended state over an extended period, the internal air was gently circulated using a fan installed at the top of the chamber. The detailed chamber structure and configuration of the particle-injection system are presented in Fig. 3.

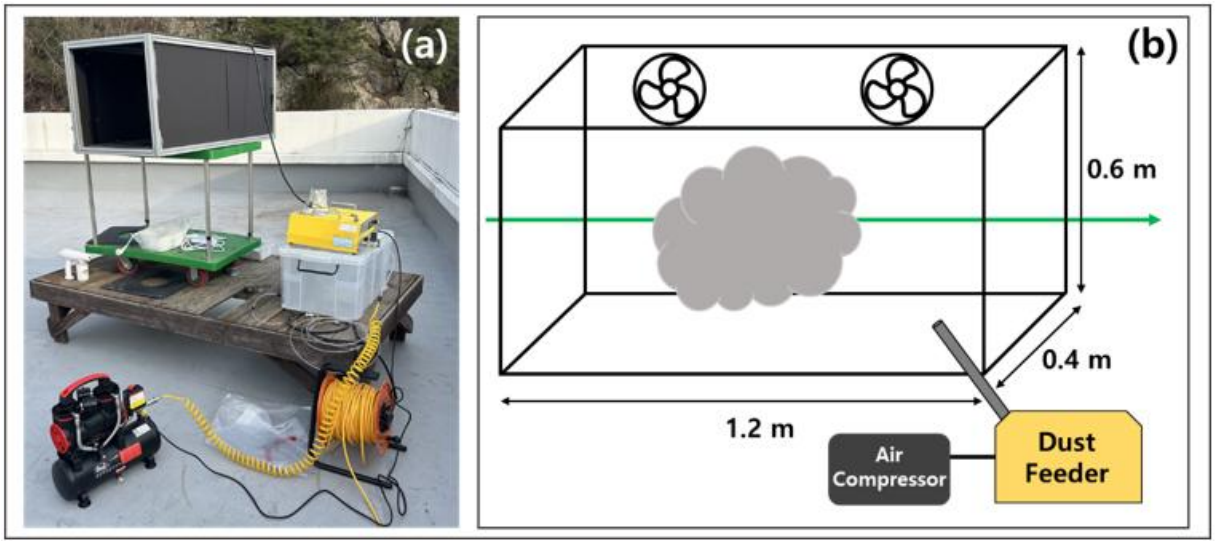

Figure 3: (a) Photograph and (b) schematic of the chamber configuration

2.3 Depolarization Ratio Calculation

In the employed LiDAR system, the received 532-nm signals are separated into their perpendicular (P_S) and parallel (P_P) components for calculating the degree of particle sphericity D_p, also defined as the ratio of the depolarized backscattered signal to the nondepolarized signal. The general formula is given by Freudenthaler et al. (2009)

$$\delta = \frac{P_S}{P_P} \quad . \tag{1}$$

Irregularly shaped particles exhibit higher depolarization ratios than rounded ones. The result calculated directly from raw signals is the total D_p in a mixed state of background aerosols (hereafter referred to as $<D_p>$). The intrinsic D_p of pure graphite must then be extracted through a mathematical retrieval process.

This study analyzes the characteristics of graphite particles using the backscatter coefficients of the parallel and perpendicular polarization signals. Specifically, the parallel (L_G^P) and perpendicular (L_G^S) LiDAR signals from the graphite injected into the

https://doi.org/10.5194/egusphere-2026-2900
Preprint. Discussion started: 10 August 2026

chamber are expressed as functions of the background aerosol backscatter coefficients (β_B^P, β_B^S) and the graphite backscatter coefficients (β_G^P, β_G^S) (Klett, 1981):

$$L_G^P(R) = E_0 \frac{\beta_G^P + \beta_B^P}{R^2} \cdot e^{-2\int \alpha(r')dr'}, \quad (2)$$

$$L_G^S(R) = E_0 \frac{\beta_G^S + \beta_B^S}{R^2} \cdot e^{-2\int \alpha(r')dr'}, \quad (3)$$

where E_0 is the laser energy, R is the measurement distance, and $\alpha(r')$ is the extinction coefficient along the path.

The ratio of these two signals represents the total mixed depolarization ratio $<D_p>$. Note that this division cancels the distance-dependent attenuation and system constants:

$$< Dp > = \frac{L_G^S}{L_G^P} = \frac{\beta_G^S + \beta_B^S}{\beta_G^P + \beta_B^P}. \quad (4)$$

To extract the intrinsic depolarization ratio of pure graphite ($Dp_G = \beta_G^S/\beta_G^P$), the numerator and denominator of the right side of Eq. (4) are divided by the parallel backscatter coefficient of graphite (β_G^P). Assuming 0.03 as the depolarization ratio of the background aerosol (Bohlmann et al., 2021), we can write $\beta_B^S = 0.03 \times \beta_B^P$ to obtain

$$< Dp > = \frac{\frac{0.03 \times \beta_B^P}{\beta_G^P} + Dp_G}{\frac{\beta_B^P}{\beta_G^P} + 1}. \quad (5)$$

The ratio of backscatter coefficients (β_B^P / β_G^P) can be replaced by the ratio of the measured LiDAR signals. As the background signal L_B^P is proportional to β_B^P, and the graphite-only signal is proportional to $L_G^P - L_B^P$, this term can be expressed as $\frac{L_B^P/L_G^P}{1-(L_B^P/L_G^P)}$. Substituting this relationship into Eq. (5) and rearranging, the final intrinsic depolarization ratio of graphite Dp_G is derived as follows:

$$Dp_G = \frac{<Dp> - 0.03(\frac{L_B^P}{L_G^P})}{1 - (\frac{L_B^P}{L_G^P})}. \quad (6)$$

Using this formula, we can distinguish and quantify the intrinsic properties of the graphite particles.

https://doi.org/10.5194/egusphere-2026-2900
Preprint. Discussion started: 10 August 2026

2.4 Data Processing and Retrieval Procedure

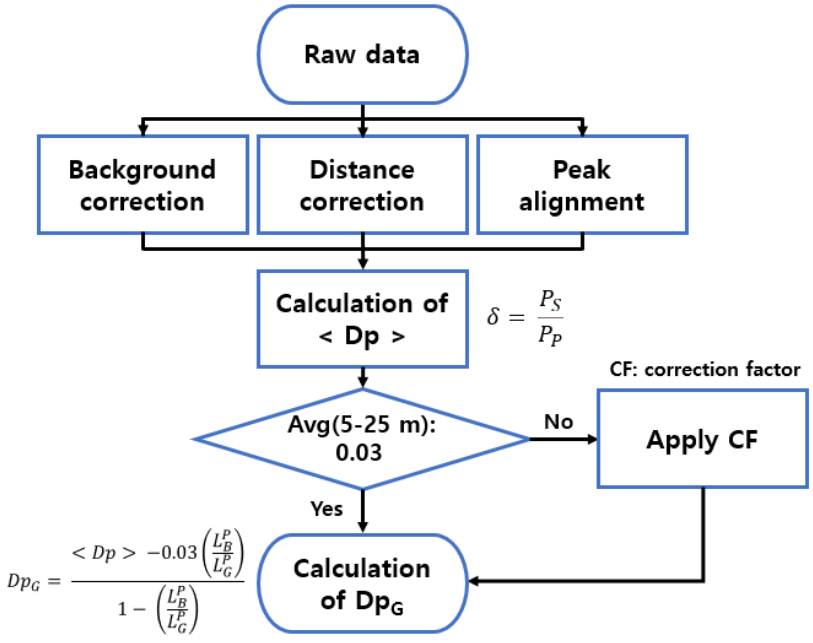

Figure 4: Flowchart of data processing and retrieval.

Figure 4 illustrates the step-by-step flowchart of LiDAR signal processing and D_p calculation of graphite particles. The key stages of this procedure, which ensure reliable and accurate data acquisition, are outlined below:

1. **Raw data**: Collects the original signals on the oscilloscope during the experiment, marking the initial stage of data analysis. All subsequent preprocessing tasks are based on these data.
2. **Distance correction**: Corrects errors caused by misidentifications of noise generated during laser emission as distance, enhancing the accuracy of the LiDAR–chamber distance.
3. **Peak alignment**: Resolves discrepancies between the peak positions of the 532P and 532S signals through cross-correlation alignment. This process improves the data accuracy by minimizing phase mismatch.
4. **Average D_p calculation**: Calculates the $<D_p>$ of the ambient air in the spatial range of 5 to 25 m from the LiDAR system (i.e., in front of the chamber). This spatial average is calculated using the continuous data points acquired at the system's 0.03-m spatial resolution. This value represents the baseline D_p of the surrounding atmospheric aerosols.
5. **Correction factor calculation**: Derives the correction factor (CF) by which the calculated average background value is adjusted to 0.03 (the standard reference for spherical aerosols).
6. Graphite D_p calculation: Multiplies the total mixed depolarization ratio by the CF to finalize the calibration. Applying the retrieval equation, this step then calculates the intrinsic Dp_G of the graphite.

https://doi.org/10.5194/egusphere-2026-2900
Preprint. Discussion started: 10 August 2026

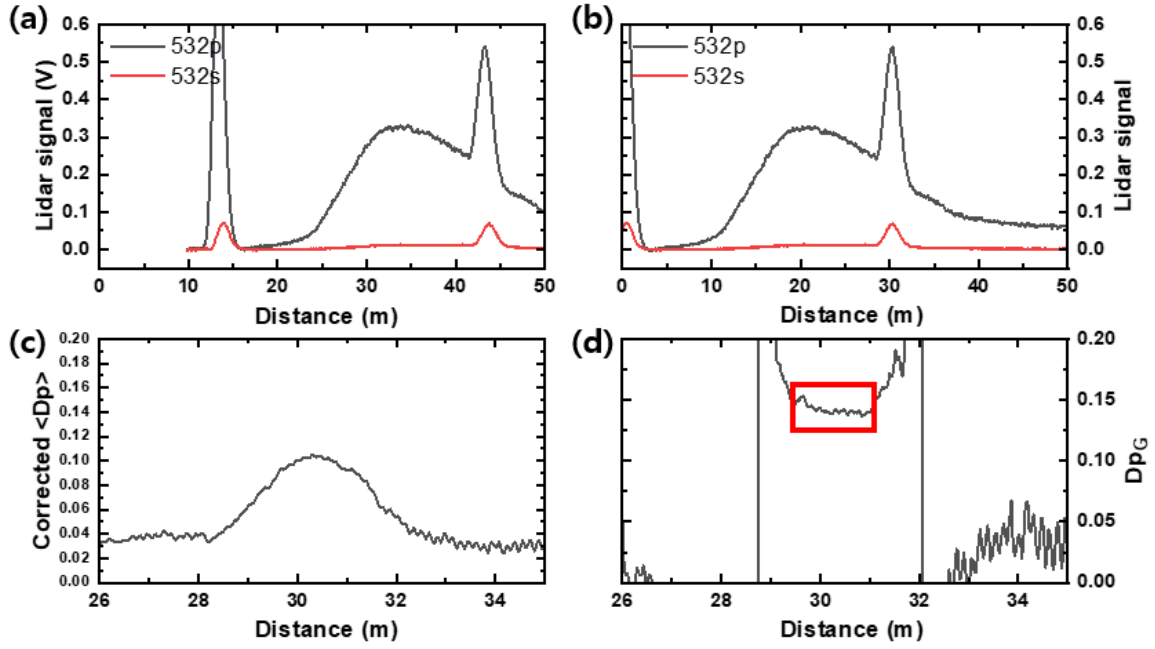

Figure 5: Visualization of step-by-step processing: (a) Raw data collection (Step 1), (b) Steps 2 and 3, (c) Steps 4 and 5, (d) final graphite D_p derivation (Step 6) (November 13, 2024, experiment).

The data analyses and correction procedures are visually summarized in Fig. 5, highlighting the essential steps from raw signal preprocessing to final derivation of the optical properties of graphite particles. Each step is designed to maximize the data precision and reliability while minimizing the effects of environmental variables through rigorous calibration.

3 Results

Graphite possesses unique structural, thermal, electrical, and mechanical properties primarily originating from its layered structure and bonding characteristics. Before the chamber experiments, the physicochemical properties of both types of sample graphite particles (Case 1: pure graphite and Case 2: steel plant-origin graphite) were determined using scanning electron microscopy (SEM) and energy dispersive X-ray spectroscopy (EDS). The compositional EDS results are shown in Table 2. The pure graphite powder (Case 1) was composed of high-purity carbon, accounting for 89.03% by weight and approximately 92.02% by atomic ratio. The graphite generated during the steelmaking process (Case 2) exhibited a much lower carbon content (50.45% by weight, 64.46% by atomic ratio) and a notably high oxygen content (31.89% by weight), indicating a substantially higher level of impurities than in Case 1. This finding suggests that graphite originating from the steel plant was severely oxidized or became mixed with other metallic PM during high-temperature thermodynamic processes.

https://doi.org/10.5194/egusphere-2026-2900
Preprint. Discussion started: 10 August 2026

Table 2: EDS-derived elemental compositions of Case 1 (pure graphite) and Case 2 (steel plant-origin graphite)

Case 1. Pure Graphite				**Case 2. Steel plant-origin graphite**			
Element	K Ratio	Wt %	Atomic %	Element	K Ratio	Wt %	Atomic %
C	0.47952	89.03	92.02	C	0.18748	50.45	64.46
				O	0.07072	31.89	30.59
O	0.00871	9.86	7.65	Al	0.00087	0.09	0.05
				Si	0.00077	0.07	0.04
Si	0.00397	0.38	0.17	S	0.00100	0.07	0.03
				Ca	0.00562	0.34	0.13
Fe	0.00794	0.73	0.16	Cr	0.00246	0.14	0.04
				Fe	0.26218	16.95	4.66
Total		100.00	100.00	Total		100.00	100.00

The morphological characteristics of the particles were derived from SEM images obtained at the Korea Institute of Energy Research. Imaging was performed in secondary electron detection mode at an accelerating voltage of 5.0 kV, a working distance of 10.1 mm, and magnifications of 2,500× and 3,000×.

Both samples exhibited the characteristic layered structure of crystalline graphite (Fig. 6) but distinctly differed in their structural development and surface roughness. The pure graphite particles (Fig. 6a) presented a typical nonspherical plate-like structure dominated by smooth basal planes and sharp edges formed through mechanical exfoliation. These observations align perfectly with theoretical expectation: graphite forms strong covalent bonds within layers, while weak van der Waals forces between layers maintain a loosely stacked platy structure. Furthermore, the pure graphite particles ranged from approximately 50 to 75 μm in size. Consistent with this observation, Lee et al. (2015) empirically found that graphite used in industrial processes can be physically degraded by thermal stress or mechanical friction, reducing its particle size to below 75 μm. Conversely, the steel plant-origin particles (Fig. 6b) formed relatively large, aggregated bulk structures ranging from 50 to 150 μm. The particle surfaces were rendered extremely rough by attached submicron particles, presumed as by-products of other processes.

https://doi.org/10.5194/egusphere-2026-2900
Preprint. Discussion started: 10 August 2026

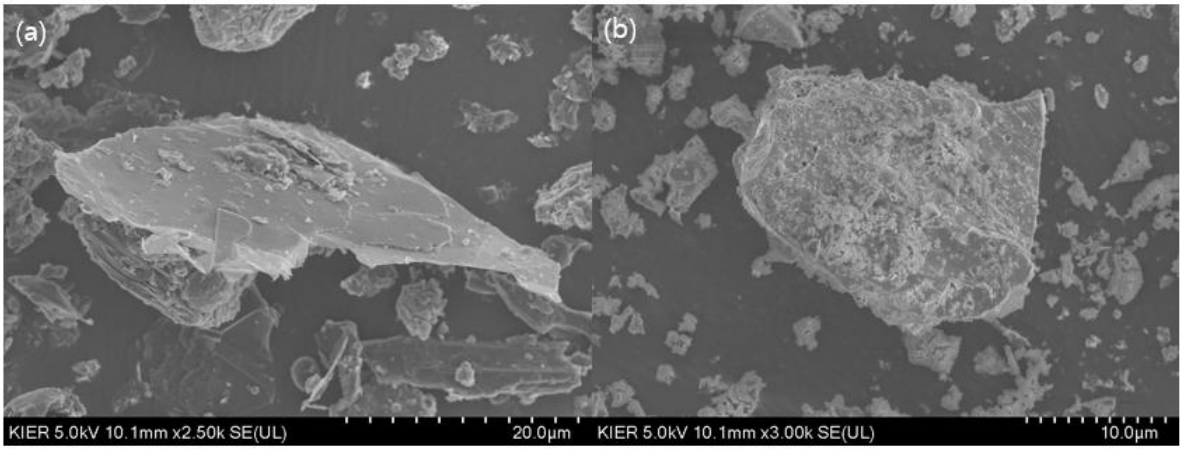

Figure 6: SEM images of (a) pure graphite particles and (b) steel plant-origin graphite particles.

The morphological analysis revealed a pronounced layered structure and high nonsphericity. When dispersed in the atmosphere, such particles can largely alter the polarization states of incoming LiDAR beams. Here, the optical properties of the graphite particles were quantified through repeated experiments within a controlled chamber environment, ultimately compiling a robust dataset of 24 experimental sessions to verify statistical reliability.

Figure 7 sequentially displays the depolarization ratio data derived from individual experimental sessions. The total apparent depolarization ratio ($<D_p>$) was measured in the mixed state of background aerosols and graphite inside the chamber. The intrinsic depolarization ratio of graphite (Dp_G) was extracted via the mathematical correction algorithm. The total depolarization ratio slightly fluctuated across sessions, reflecting variations in background concentration, but the corrected Dp_G presents a highly stable, constant horizontal distribution across all 24 data sets. This result confirms that the applied correction methodology can accurately and precisely isolate the intrinsic optical constants of graphite, irrespective of changes in injection concentration or background environmental interference.

https://doi.org/10.5194/egusphere-2026-2900
Preprint. Discussion started: 10 August 2026

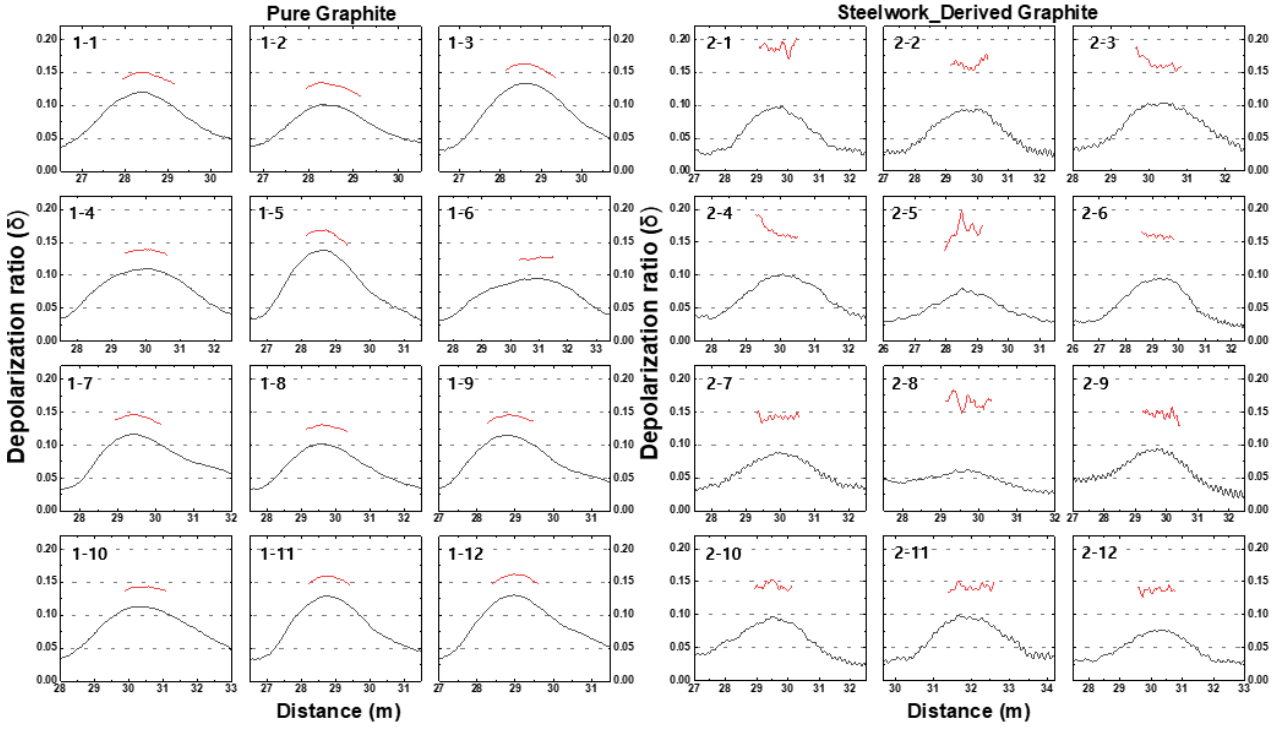

Figure 7: Comparison of total mixed (black) and intrinsic graphite (red) depolarization ratios of the two graphite samples.

Figure 8 shows the statistical processing results of the 24 experimental datasets. Plotted are the average depolarization ratios and error margins of each sample. The average D_p was calculated as 0.15 ± 0.01 for pure graphite (Case 1) and 0.16 ± 0.03 for the steel plant-originated particles (Case 2). The averages of the two samples agreed within a margin of 0.01, a highly meaningful finding in atmospheric optics. In particular, it demonstrates that polarization scrambling on the graphite particles, even on graphite generated in actual steel plants with numerous impurities and high surface roughness, is fundamentally driven by the inherent platy crystal structure and strong non-sphericity of graphite. However, the standard deviation was approximately three times larger in Case 2 than in Case 1, owing to the large size heterogeneity (50–150 μm) of particles emitted in real industrial environments and the additional scattering variability caused by surface attachments. Nevertheless, the two sets of averages were statistically consistent, confirming the established D_p (0.15) as a highly reliable optical fingerprint of graphite within complex real-world steel plant atmospheres.

https://doi.org/10.5194/egusphere-2026-2900
Preprint. Discussion started: 10 August 2026

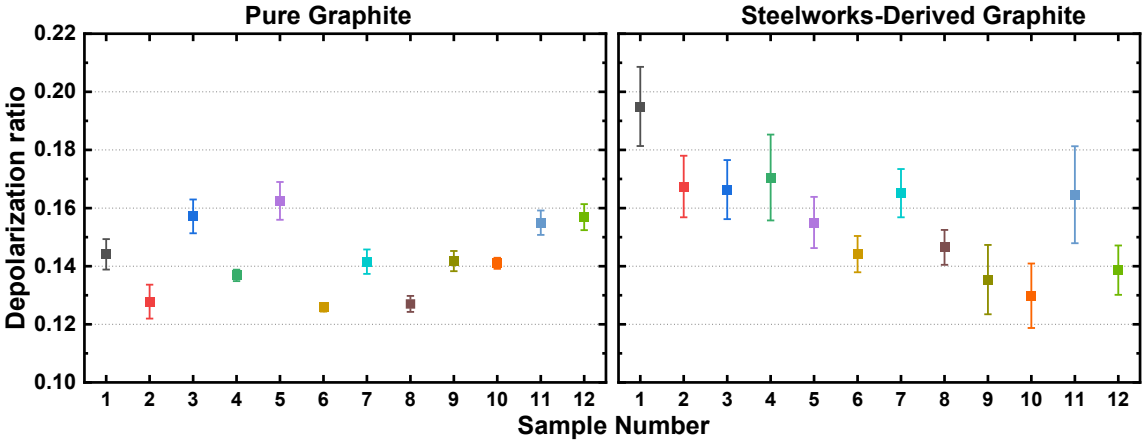

Figure 8: Case-by-case comparison of average depolarization ratios (symbols) and error margins (bars)

Figure 9 compares the graphite D_p measured in this study with those of major aerosol types reported in the literature. In general, desert dust aerosols exhibit high D_p ratios (0.25 to 0.35), mixed aerosol groups present intermediate D_p values (0.10 to 0.23), and pollution aerosols originating from urban emissions or biomass burning yield low D_p values (< 0.05) (Baars et al., 2016; Bohlmann et al., 2018; Burton et al., 2015; Filioglou et al., 2020; Floutsi et al., 2022; Gross et al., 2012; Groß et al., 2011; Janicka et al., 2017; Nepomuceno Pereira et al., 2014; Preißler et al., 2011; Rittmeister et al., 2017). The D_p of graphite measured in this study (~0.15–0.16) falls into an independent domain clearly distinguishable from the major global aerosol groups. This result clarifies the strong potential of D_p as a primary indicator of graphite originating from steel plants, promising the optical isolation and identification of such particles among diverse atmospheric aerosols.

https://doi.org/10.5194/egusphere-2026-2900
Preprint. Discussion started: 10 August 2026

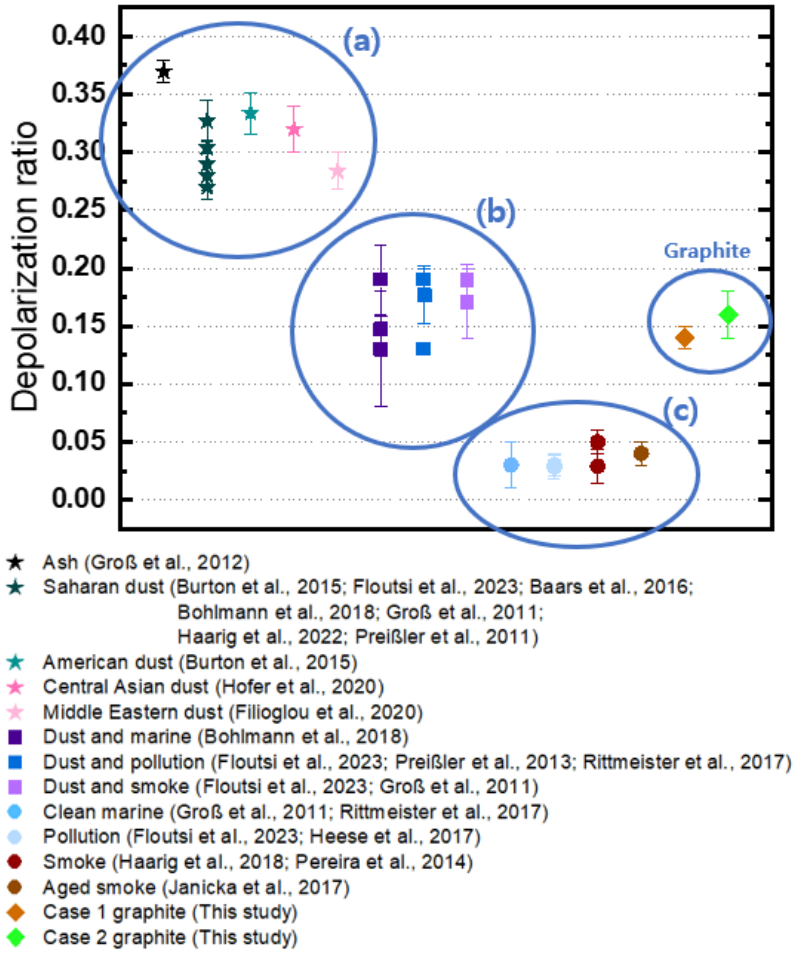

Figure 9: Depolarization ratios by aerosol type: (a) dust group, (b) mixed dust, and (c) pollution group. The graphites tested in the present study form a separate group labeled "Graphite."

4 Conclusion

To determine the unique optical properties of graphite fugitive dust emitted from steelmaking processes, establishing a scientific foundation for its remote identification, the authors measured the depolarization ratio of pure graphite particles at 532 nm. Precise measurements were achieved using a custom-built near-field polarization LiDAR system and an aerosol chamber.

The study identified an intrinsic depolarization ratio (0.15–0.16) of graphite that falls into a distinct optical regime, clearly separated from those of typical desert dust (> 0.25) and anthropogenic pollution particles (< 0.05). Repeated independent experiments yielded highly reproducible and reliable data. The depolarization ratios of both pure graphite samples and actual particles collected from steel plants aligned within the margin of error, scientifically validating the field applicability of these findings.

https://doi.org/10.5194/egusphere-2026-2900
Preprint. Discussion started: 10 August 2026

This research is also valuable from a methodological perspective. The custom-built LiDAR system effectively overcame the geometric overlap problem—a chronic limitation of conventional LiDAR—by implementing a 30-m separation distance and ultrahigh spatial resolution (0.03 m). The developed analytical framework can precisely extract the fine optical properties of specific particle groups in controlled environments.

The intrinsic depolarization ratio of graphite, here quantified for the first time, provides a foundational baseline for developing smart monitoring technologies that can selectively track and manage specific fugitive dust types generated in industrial zones such as steel plants. When applied to various other industrial dust emissions in future studies, this methodology is expected to contribute to the advancement of fugitive-dust management technologies.

Data availability

Data will be made available upon reasonable request.

Author contributions

GP conceptualized the study, established the methodology, performed the formal analysis, and wrote the original draft. DK developed the software and validated the measurement equipment. GN co-supervised the research direction, validated the experimental data, and reviewed and edited the final manuscript. YN administered the project, acquired funding, supervised the research direction, and reviewed and edited the final manuscript.

Competing interests

The authors declare that they have no conflict of interest.

Acknowledgements

The authors would like to thank the Korea Institute of Energy Research (KIER) for their assistance with the scanning electron microscopy (SEM) imaging. We also acknowledge the use of air-quality data from the Airkorea network of the Ministry of Environment and meteorological data from the Korea Meteorological Administration.

Financial support

This work was supported by grants from the National Institute of Environmental Research (NIER), funded by the Ministry of Environment (ME) of the Republic of Korea (NIER-2025-04-02-024 and NIER-2025-01-01-012).

https://doi.org/10.5194/egusphere-2026-2900
Preprint. Discussion started: 10 August 2026

Review statement

References

Amodio, M., Andriani, E., Dambruoso, P., de Gennaro, G., Di Gilio, A., Intini, M., Palmisani, J., and Tutino, M.: A monitoring strategy to assess the fugitive emission from a steel plant, Atmos. Environ., 79, 455-461, 2013.

Baars, H., Kanitz, T., Engelmann, R., Althausen, D., Heese, B., Komppula, M., Preißler, J., Tesche, M., Ansmann, A., and Wandinger, U.: An overview of the first decade of Polly NET: an emerging network of automated Raman-polarization lidars for continuous aerosol profiling, Atmos. Chem. Phys., 16, 5111-5137, 2016.

Bohlmann, S., Baars, H., Radenz, M., Engelmann, R., and Macke, A.: Ship-borne aerosol profiling with lidar over the Atlantic Ocean: from pure marine conditions to complex dust–smoke mixtures, Atmos. Chem. Phys., 18, 9661-9679, 2018.

Bohlmann, S., Shang, X., Vakkari, V., Giannakaki, E., Leskinen, A., Lehtinen, K., Pätsi, S., and Komppula, M.: Lidar depolarization ratio of atmospheric pollen at multiple wavelengths, Atmos. Chem. Phys. Discuss., 2020, 1-24, 2020.

Bohlmann, S., Shang, X., Vakkari, V., Giannakaki, E., Leskinen, A., Lehtinen, K. E., Pätsi, S., and Komppula, M.: Lidar depolarization ratio of atmospheric pollen at multiple wavelengths, Atmos. Chem. Phys., 21, 7083-7097, 2021.

Burton, S., Hair, J., Kahnert, M., Ferrare, R., Hostetler, C., Cook, A., Harper, D., Berkoff, T., Seaman, S., and Collins, J.: Observations of the spectral dependence of linear particle depolarization ratio of aerosols using NASA Langley airborne high-spectral resolution laser, Atmos. Chem. Phys., 15, 13453-13473, 2015.

Doherty, R. M., Heal, M. R., and O'Connor, F. M.: Climate change impacts on human health over Europe through its effect on air quality, Environ. Health, 16, 33-44, 2017.

Dusseldorp, A., Kruize, H., Brunekreef, B., Hofschreuder, P., De Meer, G., and Van Oudvorst, A.: Associations of PM10 and airborne iron with respiratory health of adults living near a steel factory, Am. J. Respir. Crit. Care Med., 152, 1932-1939, 1995.

Eberhard, W. and McNice, G.: Versatile lidar for atmospheric studies, including plume dispersion, clouds, and stratospheric aerosol, J. Atmos. Ocean. Technol., 3, 614-622, 1986.

Filioglou, M., Giannakaki, E., Backman, J., Kesti, J., Hirsikko, A., Engelmann, R., O'Connor, E., Leskinen, J. T., Shang, X., and Korhonen, H.: Optical and geometrical aerosol particle properties over the United Arab Emirates, Atmos. Chem. Phys., 20, 8909-8922, 2020.

Floutsi, A. A., Baars, H., Engelmann, R., Althausen, D., Ansmann, A., Bohlmann, S., Heese, B., Hofer, J., Kanitz, T., and Haarig, M.: DeLiAn–a growing collection of depolarization ratio, lidar ratio and Ångström exponent for different aerosol types and mixtures from ground-based lidar observations, Atmos. Meas. Tech. Discuss., 2022, 1-39, 2022.

Freudenthaler, V., Esselborn, M., Wiegner, M., Heese, B., Tesche, M., Ansmann, A., Müller, D., Althausen, D., Wirth, M., and Fix, A.: Depolarization ratio profiling at several wavelengths in pure Saharan dust during SAMUM 2006, Tellus B, 61, 165-179, 2009.

https://doi.org/10.5194/egusphere-2026-2900
Preprint. Discussion started: 10 August 2026

Groß, S., Freudenthaler, V., Schepanski, K., Toledano, C., Schäfler, A., Ansmann, A., and Weinzierl, B.: Optical properties of long-range transported Saharan dust over Barbados as measured by dual-wavelength depolarization Raman lidar measurements, Atmos. Chem. Phys., 15, 11067-11080, 2015.

Groß, S., Tesche, M., Freudenthaler, V., Toledano, C., Wiegner, M., Ansmann, A., Althausen, D., and Seefeldner, M.: Characterization of Saharan dust, marine aerosols, and mixtures of biomass-burning aerosols and dust by means of multi-wavelength depolarization and Raman lidar measurements during SAMUM 2, Tellus B, 63, 706-724, 2011.

Gross, S., Freudenthaler, V., Wiegner, M., Gasteiger, J., Geiss, A., and Schnell, F.: Dual-wavelength linear depolarization ratio of volcanic aerosols: Lidar measurements of the Eyjafjallajökull plume over Maisach, Germany, Atmos. Environ., 48, 85-96, 2012.

Hanoa, R.: Graphite pneumoconiosis: A review of etiologic and epidemiologic aspects, Scand. J. Work Environ. Health, 303-314, 1983.

Janicka, L., Stachlewska, I. S., Veselovskii, I., and Baars, H.: Temporal variations in optical and microphysical properties of mineral dust and biomass burning aerosol derived from daytime Raman lidar observations over Warsaw, Poland, Atmos. Environ., 169, 162-174, 2017.

Jia, J., Cheng, S., Yao, S., Xu, T., Zhang, T., Ma, Y., Wang, H., and Duan, W.: Emission characteristics and chemical components of size-segregated particulate matter in iron and steel industry, Atmos. Environ., 182, 115-127, 2018.

Klett, J. D.: Stable analytical inversion solution for processing lidar returns, Appl. Opt., 20, 211-220, 1981.

Lee, S.-M., Kang, D.-S., and Roh, J.-S.: Bulk graphite: materials and manufacturing process, Carbon Lett., 16, 135-146, 2015.

Ma, X., Wang, C., Han, G., Ma, Y., Li, S., Gong, W., and Chen, J.: Regional atmospheric aerosol pollution detection based on LiDAR remote sensing, Remote Sens., 11, 2339, 2019.

Pereira, S., Preißler, J., Guerrero-Rascado, J. L., Silva, A. M., and Wagner, F.: Forest fire smoke layers observed in the free troposphere over Portugal with a multiwavelength Raman lidar: Optical and microphysical properties, ScientificWorldJournal, 2014, 421838, 2014.

Noh, Y. M., Müller, D., Lee, H., and Choi, T. J.: Influence of biogenic pollen on optical properties of atmospheric aerosols observed by lidar over Gwangju, South Korea, Atmos. Environ., 69, 139-147, 2013a.

Noh, Y. M., Lee, H., Mueller, D., Lee, K., Shin, D., Shin, S., Choi, T., Choi, Y., and Kim, K.: Investigation of the diurnal pattern of the vertical distribution of pollen in the lower troposphere using LIDAR, Atmos. Chem. Phys., 13, 7619-7629, 2013b.

Pal, S., Behrendt, A., Radlach, M., Schaberl, T., and Wulfmeyer, V.: Eye-safe scanning aerosol lidar at 355 nm, Reviewed and Revised Papers of the 23rd International Laser Radar Conference (ILRC 2006), 1-4.

Palm, S. P., Melfi, S., and Carter, D. L.: New airborne scanning lidar system: applications for atmospheric remote sensing, Appl. Opt., 33, 5674-5681, 1994.

Preißler, J., Wagner, F., Pereira, S., and Guerrero-Rascado, J.: Multi-instrumental observation of an exceptionally strong Saharan dust outbreak over Portugal, J. Geophys. Res. Atmos., 116, 2011.

Rahman, M.: Pneumoconiosis: Cumulative global research output, Indian J. Biochem. Biophys., 59, 224-228, 2022.

https://doi.org/10.5194/egusphere-2026-2900
Preprint. Discussion started: 10 August 2026

Rittmeister, F., Ansmann, A., Engelmann, R., Skupin, A., Baars, H., Kanitz, T., and Kinne, S.: Profiling of Saharan dust from the Caribbean to western Africa–Part 1: Layering structures and optical properties from shipborne polarization/Raman lidar observations, Atmos. Chem. Phys., 17, 12963-12983, 2017.

Sakai, T., Nagai, T., Nakazato, M., Mano, Y., and Matsumura, T.: Ice clouds and Asian dust studied with lidar measurements of particle extinction-to-backscatter ratio, particle depolarization, and water-vapor mixing ratio over Tsukuba, Appl. Opt., 42, 7103-7116, 2003.

Sassen, K. and Benson, S.: A midlatitude cirrus cloud climatology from the Facility for Atmospheric Remote Sensing. Part II: Microphysical properties derived from lidar depolarization, J. Atmos. Sci., 58, 2103-2112, 2001.

Scollo, S., Boselli, A., Coltelli, M., Leto, G., Pisani, G., Spinelli, N., and Wang, X.: Monitoring Etna volcanic plumes using a scanning LiDAR, Bull. Volcanol., 74, 2383-2395, 2012.

Shimizu, A., Nishizawa, T., Jin, Y., Kim, S.-W., Wang, Z., Batdorj, D., and Sugimoto, N.: Evolution of a lidar network for tropospheric aerosol detection in East Asia, Opt. Eng., 56, 031219-031219, 2017.

Shin, J., Sim, J., Tesche, M., Yoon, J., Kim, D., and Noh, Y.: Machine learning-based retrieval of aerosol size and hygroscopicity using horizontal scanning LiDAR and PM data, npj Clim. Atmos. Sci., 2025.

Taylor, H. A., Jr.: Mineral Facts and Problems: 1985 Edition, 339-348, 1985.

Uthe, E. E.: Application of surface-based and airborne lidar systems for environmental monitoring, J. Air Pollut. Control Assoc., 33, 1149-1155, 1983.

Wang, X., Pan, H., Guo, K., Yang, X., and Luo, S.: The evolution of LiDAR and its application in high precision measurement, IOP Conf. Ser. Earth Environ. Sci., 012008.

Xian, J., Sun, D., Xu, W., Han, Y., Zheng, J., Peng, J., and Yang, S.: Urban air pollution monitoring using scanning Lidar, Environ. Pollut., 258, 113696, 2020.

Xie, C., Zhao, M., Wang, B., Zhong, Z., Wang, L., Liu, D., and Wang, Y.: Study of the scanning lidar on the atmospheric detection, J. Quant. Spectrosc. Radiat. Transf., 150, 114-120, 2015.